

A study of B Meson lifetime at the KEK B factory

Nakadaira Takeshi¹

Jan, 11, 2000

¹nakadair@tkybell1.phys.s.u-tokyo.ac.jp

Abstract

The KEK B factory has the advantage for the measurement of B meson lifetimes in several points. We can reduce the statistical error in the lifetime measurement because a large amount of B mesons is provided by accelerator. And B mesons produced by asymmetric e^+e^- collider at the $\Upsilon(4S)$ resonance have the fixed Lorentz boost factor determined by the accelerator conditions. We study on lifetime B meson making use of these advantages. We perform a simulation of the experiment by treating Monte Carlo events corresponding to $4[\text{fb}^{-1}]$ as real data. We reconstruct the vertices of 2178 $B^0\bar{B}^0$ pair and 2677 B^+B^- pair candidate thorough $B \rightarrow D^*\ell\nu_\ell$ modes. And we perform a unbinned maximum likelihood fit to the decay length difference of BB pair and consistently obtained the lifetimes B meson lifetime at the $\tau_{B^0} = 1.74 \pm 0.087[\text{ps}]$ and $\tau_{B^+} = 1.50 \pm 0.10[\text{ps}]$ where input values are $\tau_{B^0} = 1.56[\text{ps}]$ and $\tau_{B^+} = 1.62[\text{ps}]$. We also analyze the real data from the BELLE detector corresponding to $0.2[\text{fb}^{-1}]$ and obtained the distributions of the decay length difference of BB pair.

Contents

1	Introduction	1
2	BELLE experiment	2
2.1	Overview	2
2.2	KEKB accelerator	3
2.3	BELLE detector	4
2.3.1	Overview	4
2.3.2	Silicon Vertex Detector (SVD)	5
2.3.3	Central Drift Chamber (CDC)	6
2.3.4	Aerogel Čerenkov Counter (ACC)	7
2.3.5	Time of Flight Counter (TOF)	8
2.3.6	Electromagnetic Calorimeter (ECL)	9
2.3.7	Super-conducting Solenoid	10
2.3.8	K_L/μ Detector (KLM)	11
2.4	Simulation software for the BELLE detector	11
2.4.1	Overview	11
2.4.2	Event generator	12
2.4.3	Detector simulation	13
2.4.4	Reconstruction software	13
3	Lifetime measurement	15
3.1	Overview	15
3.2	Event reconstruction	16
3.2.1	Reconstruction of B meson	16
3.3	Vertex reconstruction	26
3.4	Lifetime fit to signal	30
3.5	Background estimation	31
3.6	Lifetime fit with background	33
4	Data Analysis	37

5	Conclusions	41
A	Remaining problems and future plans	42

Chapter 1

Introduction

We study charged and neutral B meson lifetimes at the B factory of High Energy Accelerator Research organization (KEK). The precise measurement of B hadron lifetimes is important to study of the weak decays of b-quark and to determine Cabibbo-Kobayashi-Maskawa matrix (CKM) element $|V_{cb}|$. In a simple spectator model B meson lifetimes are degenerate, i.e. lifetimes of B^0 , B^+ and B_s are exactly same. In general, the difference of lifetime between neutral and charged charmed mesons is explained by the non-spectator decay such as the annihilation and the W -exchange processes, and the final-state interference effects. Although the lifetimes of D^+ and D^0 mesons are different by a factor of 2.5, the difference of B meson lifetimes is expected to be less than 10% because of the large mass of the b-quark. In a heavy quark expansion theory the lifetime difference of mesons depends on terms of the order of $1/m_b^3$. Precise measurement of the neutral and charged B meson lifetimes can probe the decay mechanism beyond simple spectator models, and provide a quantitative test for theoretical predictions.

The measurements of B^+ and B^- meson lifetimes have already been performed by LEP, SLD and CDF experiments. The current world average value is 1.56 ± 0.04 [ps] for B^0 and 1.65 ± 0.04 [ps] for B^+ [2]. Since a large amount of B mesons (10^8 $B^0\overline{B}^0$ or B^+B^- pairs a year) are produced with small background in the B factory, it is possible to reduce the statistical error.

The B meson lifetime measurement at the B factory also play a key role in understanding vertexing performance of the detector. Observation of CP violation is a main goal of the B factory and it requires a precise measurements of B decay vertices. B meson lifetimes can be measured at relatively small statistics. Systematic effects related with vertexing can be evaluated at the same time.

Chapter 2

BELLE experiment

2.1 Overview

The goal of the BELLE experiments[1] is to perform definitive tests of the Kobayashi-Maskawa Model predictions for CP violations in B meson decays. Since the first observation of CP violation in the neutral kaon system in 1964, an enormous amount of theoretical work has been done to understand the phenomenon. In 1973, Kobayashi and Maskawa (KM) noted that CP violation could be accommodated in the framework of the Standard Model (SM) only if there were at least six quark flavors, twice the number of quark flavors known at the time. The subsequent discoveries of c , b and t quarks have proven the six-quark KM hypothesis, and the KM model for CP violation is now considered to be an essential part of the SM. In 1980, Sanda and Cater pointed out that the KM model contained a possibility of rather sizable CP violating asymmetries in certain decay modes of B mesons. Observations of CP violations in B meson decays would be a confirmation of the KM model. The largest observable effects are expected to show up in the difference of the decay rates between B^0 and \bar{B}^0 mesons to the same CP eigenstate. The measurements of CP asymmetries using $B^0\bar{B}^0$ pairs from $\Upsilon(4S)$ (the resonance state of $b\bar{b}$) decays must be derived from comparisons of the time evolution of B^0 and \bar{B}^0 decays, because the time-integrated asymmetries vanishes in $\Upsilon(4S)$ system. An asymmetric e^+e^- storage ring at the $\Upsilon(4S)$ resonance is most favored because it boosts the B^0 mesons allowing existing vertex measurement technology to measure the $B^0\bar{B}^0$ decay time. $B^0 \rightarrow J/\Psi K_S$ mode is one of the most promising decay mode because this mode is free from background and theoretical uncertainties are small. In this mode, the

asymmetry A , is related to the CP angle ϕ_1 as

$$\begin{aligned} A(\Delta t) &= \frac{\Gamma(B^0(\Delta t) \rightarrow J/\psi K_S) - \Gamma(\bar{B}^0(\Delta t) \rightarrow J/\psi K_S)}{\Gamma(B^0(\Delta t) \rightarrow J/\psi K_S) + \Gamma(\bar{B}^0(\Delta t) \rightarrow J/\psi K_S)} \\ &= -\sin 2\phi_1 \sin(\Delta m_B \Delta t) \end{aligned}$$

where Δt is the proper time difference of two B meson decays and Δm_B is the mass difference of two CP eigenstates of neutral B mesons which is measured from the magnitude of B^0 - \bar{B}^0 mixing. The proper time difference Δt is given by $\Delta t \simeq \Delta z/c\beta\gamma$ where $\beta\gamma$ is the Lorentz boost factor of the $\Upsilon(4S)$ system due to the asymmetric beam energies and Δz is the distance between the two B decay vertices along the beam direction. This requires precise measurements of the B decay vertices.

the detector is also required the ability to identify the flavor of neutral B meson. The flavor of B mesons is determined from the charge of the high momentum lepton from B meson and from the number of charged Kaon tracks. Therefore the good efficiency of the Kaon identification is required in CP violation measurement. The electron and muon identification is also very important to reconstruct J/Ψ s which decay to electron pairs and to determine the flavor of the tagging side B meson. The B meson flavor decaying into $J/\Psi K_S$ is identified by the flavor on the other B meson. The B meson flavor is identified by the charge of leptons via B semileptonic decays or kaons via $b \rightarrow c \rightarrow s$ decay chain. It is essential to identify leptons and kaons for the flavor tagging.

2.2 KEKB accelerator

The KEKB accelerator is an asymmetric e^+e^- collider to produce boosted $\Upsilon(4S)$. The $\Upsilon(4S)$ produced from the collision of 8.0GeV electron with 3.5GeV positron has finite momentum ($\beta\gamma = 0.425$). $\Upsilon(4S)$ decays to $B^0\bar{B}^0$ or B^+B^- pair with the same decay fraction. the mean decay length of produced B meson would be $\sim 200\mu\text{m}$ in the lab frame. The designed luminosity of KEKB is $10^{34}[\text{cm}^{-2}\text{s}^{-1}]$ which corresponds to $10^8\Upsilon(4S)$ a year. The configuration of KEKB is shown in Figure.2.1.

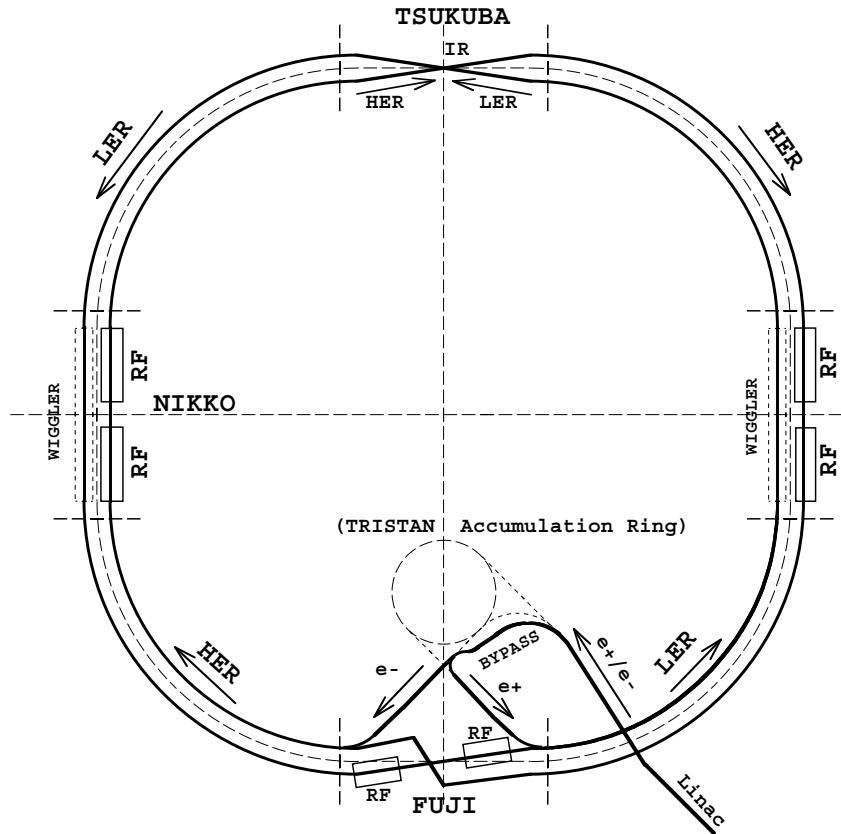


Figure 2.1: Configuration of the KEKB accelerator

2.3 BELLE detector

2.3.1 Overview

The BELLE detector consists of the seven component, namely Silicon Vertex Detector (SVD) for the measurement of the decay point of particles, Central Drift Chamber (CDC) for the measurement of the momentum of charged particles, Time Of Flight counter (TOF) and Aerogel Čerenkov Counter (ACC) for the charged particle identification, Electromagnetic Calorimeter (ECL) for the detection of electrons and photons, K_L/μ Detector (KLM) for the detection of K_L mesons and muons, and Super-conducting Solenoid. The

overview of the BELLE detector is shown in Figure. 2.2.

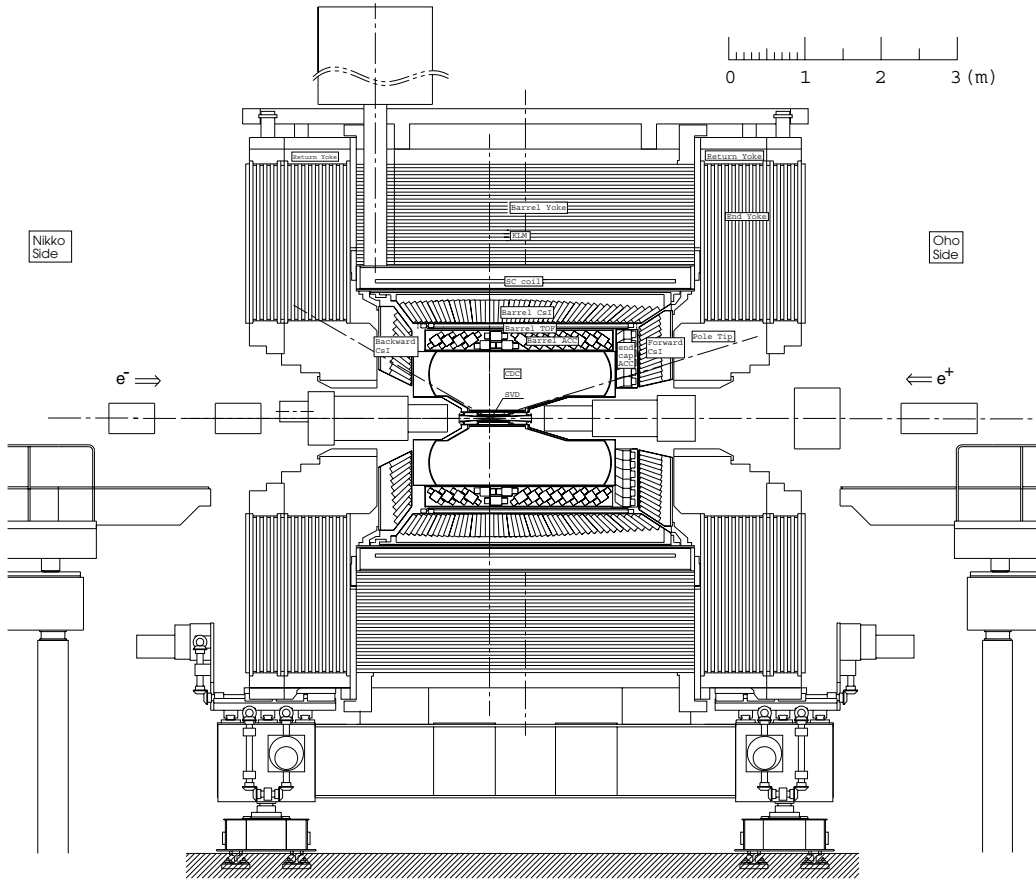


Figure 2.2: The BELLE detector

2.3.2 Silicon Vertex Detector (SVD)

The Silicon Vertex Detector (SVD) measures the decay point of the particles. The SVD consists of 102 Double-sided Silicon Micro-strip Detector (DSSD): S6939 DSSDs fabricated by Hamamatsu Photonics. They consist of 1280 sense strip and 640 readout pads on each side. The z -strip pitch is $42 \text{ } [\mu\text{m}]$ and the ϕ strip pitch is $25 \text{ } [\mu\text{m}]$. For the z -coordinate determination, a double-metal layer structure is employed to readout the signal of orthogonal z -sense strip along the the beam axis. Adjacent strip are connected to one readout trace on the second metal layer. The DSSDs are aligned to make three radial

layers at radii of 30.0, 45.5 and 60.5 [mm]. Because the dominant source of the vertex resolution degradation is multiple-Coulomb scattering, the innermost layer is designed to be placed as close to the interaction point as possible. The structure of SVD is shown Figure.2.3. Each layer is constructed from DSSDs and the front-end electronics. And the VA1 chips manufactured by IDE AS in Norway are used as the readout LSI for the DSSDs. The VA1 chip consists of 128ch pre-amplifiers, shapers, sample/hold circuits and a analog analog multiplexer. The SVD covers $23^\circ < \theta < 139^\circ$, corresponding to the angular acceptance of 86 % of 4π . The decay length difference resolution of SVD is ~ 100 [μ m].

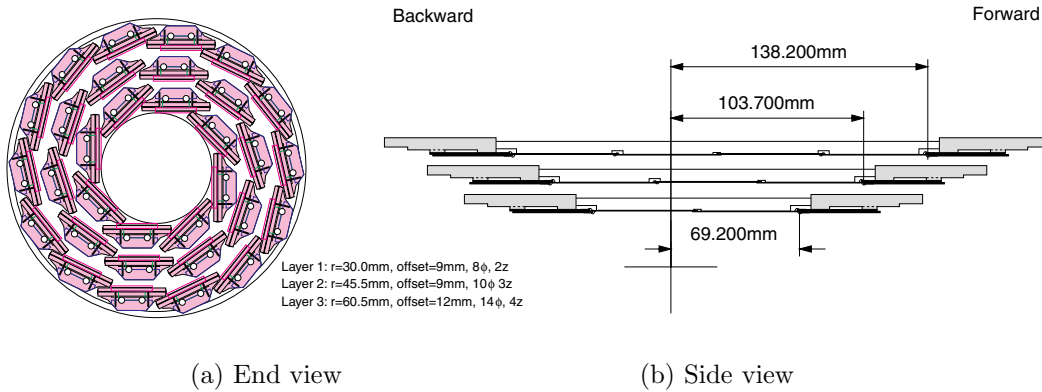


Figure 2.3: the mechanical structure of the SVD

2.3.3 Central Drift Chamber (CDC)

The Central Drift Chamber (CDC) provides charged particle tracking and dE/dx measurement for the charged particle identification as well as fast charged-track information for the trigger. The Structure of CDC is shown in Figure.2.4. CDC consists of 50 cylindrical layers of sense wires and 3 cathode strip layers. The layers of drift cells divided by the sense wires organized into 11 super-layers, where 6 of them are axial super-layers and the rest are the stereo super-layers for the measurement of z coordinate of the charged tracks. The number of readout anode wires and cathode strips are 8,400 and 1,792. A 50% Helium - 50% ethane(C_6H_6) gas mixture is filled in the chamber to minimize the multiple-coulomb scattering. The CDC covers the $17^\circ < \theta < 150^\circ$, providing angular acceptance of 92% of 4π in the $\Upsilon(4S)$ rest

frame. The expected momentum resolution is $\sigma_p/p = 0.25\sqrt{1+p^2}\%$. From the result of beam test on the prototype, the spatial resolution is expected to be 130 [μm] and the dE/dx resolution is 5.2% for 3.5[GeV] pions. This corresponds to a better than 3σ K/π separation below 0.8 [GeV] and 4σ e/π separation. e/π separation below 1[GeV/c] is very important for electron identification because the E/p method using ECL is not effective in this momentum region.

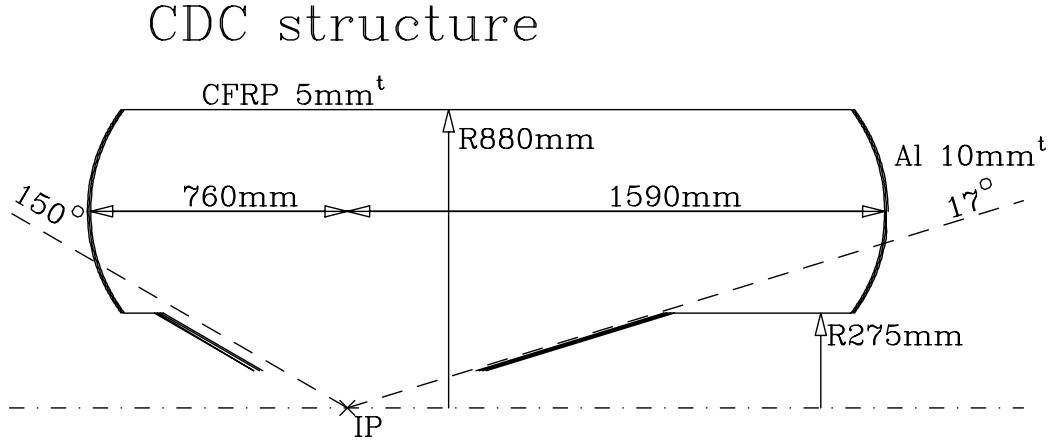


Figure 2.4: Structure of Central Drift Chamber

2.3.4 Aerogel Čerenkov Counter (ACC)

The Aerogel Čerenkov Counter (ACC) system extends the coverage for particle identification upward from 1.2[GeV/c], the upper limit of the Time of Flight system, to the kinematic limit of 2-body B decays such as $B^0 \rightarrow \pi^+\pi^-$, to $p = 2.5 \sim 3.5$ [GeV/c], depending on the polar angle. The Aerogel of the ACC is SiO_2 . The reflection index of the aerogel is chosen so that the pion produce Čerenkov light in the aerogel while the kaon does not. In general, the threshold of the Čerenkov light emission in the matter with the reflective index of n is represented using the velocity of particle β as follows:

$$n > \frac{1}{\beta} = \sqrt{1 + (m/p)^2} \quad (2.1)$$

where the particle momentum p is measured by CDC.

The ACC is divided into two part. A barrel array (BACC) covers an angular range of $34^\circ < \theta < 127^\circ$ and A forward end-cap array (EACC)

covers an angular range of $17^\circ < \theta < 34^\circ$. The BACC consists of 960 aerogel counter modules. Each aerogel counter modules consists of silica aerogel radiator and fine-mesh photo multiplier tubes (FM-PMT) to detect Čerenkov radiation. the typical aerogel radiator comprised aerogel tiles contained in a 0.2[mm] thick aluminum box. The inner surface of the box is lined with a Goretex sheet as a reflector. On BACC, Five different indices of reflection are used depending on the polar angle. The EACC consists of 228 modules of which the reflection index equals to 1.03. This eliminates the need for TOF system in end-cap region, since this reflection index gives $3\sigma K/\pi$ separation in the momentum range from 0.7 to 2.4 [GeV/c].

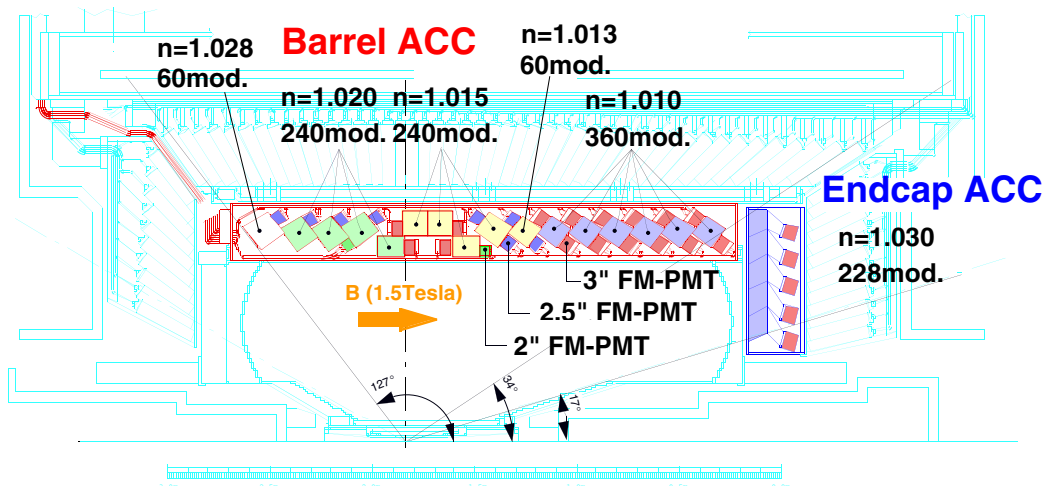


Figure 2.5: The configuration of ACC

2.3.5 Time of Flight Counter (TOF)

The Time of Flight system provide the information to separate K/π and the clean event timing signal to the BELLE trigger system. The relation between the measured flight time T , and the particle mass is as follows:

$$T = \frac{L}{c} \sqrt{1 + (m/p)^2} \quad (2.2)$$

where L is the flight length depend on TOF geometry and the particle momentum p is measured by CDC. The TOF system has a 100 [ps] time reso-

lution which corresponds to $3\sigma K/\pi$ separation up to 1.2 [GeV/c]. The TOF system comprise 64 barrel TOF/TSC modules. The figure of the TOF/TSC module is shown in Figure.2.6 .Each TOF/TSC module consists of two trapezoidally shaped TOF counters (thickness 4[mm]) and one Trigger Scintillation Counter (thickness 5[mm]). Each modules are located at $r=120$ [cm].The TOF covers an angular range of $35^\circ < \theta < 121^\circ$.

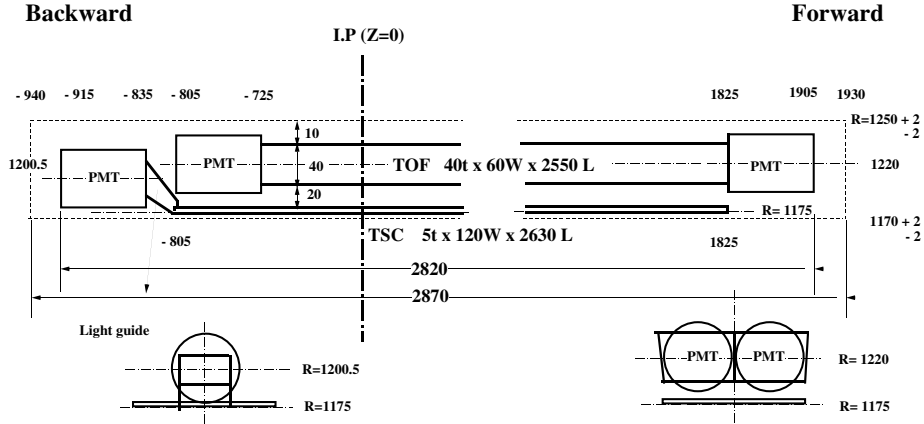


Figure 2.6: The TOF/TSC module

2.3.6 Electromagnetic Calorimeter (ECL)

The purpose of the Electromagnetic Calorimeter (ECL) is the electron identification and the detection of photons. Electrons and photons bring about the electromagnetic shower and leave a almost all energy. On the other hand kaons and pions do not bring about the the electromagnetic shower. The ratio of the energy deposit to the momentum($E/|\mathbf{p}|$) is $E/|\mathbf{p}| \sim 1$ for electrons, but $E/|\mathbf{p}| < 1$ for the other charged particles. The shower shapes of the electromagnetic shower is different from the hadronic shower. The cluster caused by the hadronic shower is spread compared to the electromagnetic shower. The ECL is based on CsI(Tl) crystal. The ECL is separated to 3 parts: the barrel part with 6624 crystals (angle coverage: $32.2^\circ < \theta < 128.7^\circ$), the forward endcap part with 1152 crystals (angle coverage: $12.4^\circ < \theta < 31.4^\circ$), and the backward endcap part with 960 crystals (angle coverage: $130.7^\circ < \theta < 155.0^\circ$). The All of the CsI(Tl) crystals are 30[cm] (16.1 radiation length) long.

The detection of photons is very important in BELLE because approximately one third of the final state particles from B meson decay is π^0 . To achieve the high π^0 reconstruction efficiency, the high sensitivity to photons is essential. The π^0 mass resolution strongly depends on the energy resolution of low energy photons. The ECL also measures the luminosity by the Bhabha scattering which yields high energy electrons. Structure of ECL is shown in Figure.2.7.

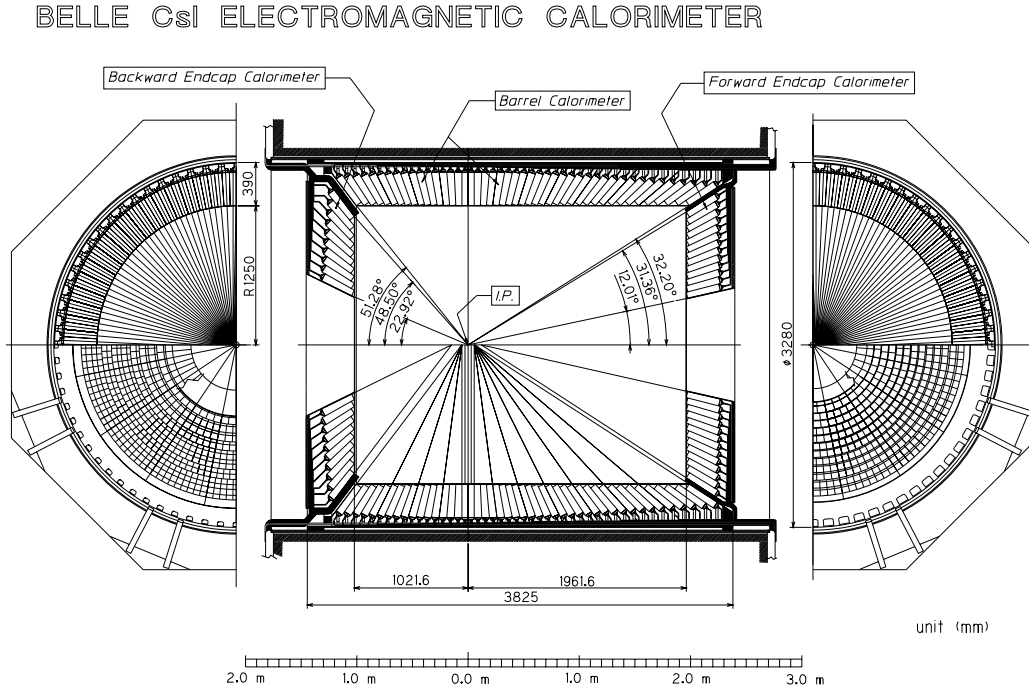


Figure 2.7: Overall configuration of Electromagnetic Calorimeter

2.3.7 Super-conducting Solenoid

A super-conducting magnet provide a magnet field strength of 1.5[T] in a cylindrical volumes of 3.4[m] in diameter and 4.4[m] in length. This field strength is chosen to minimize momentum resolution of CDC without sacrificing efficiency for low momentum tracks. The expected non-uniformity of a magnet field strength in CDC volume is 2.0%. This non-uniformity is taken into account in the tracking software.

2.3.8 K_L/μ Detector (KLM)

The K_L and Muon Detector (KLM) is designed to detect K_L and muons with momenta above 600 [MeV/c]. The muon identification by the KLM is very important to reconstruct J/Ψ s which decay to muon pairs and to identify the flavor tagging B meson in the CP violation measurement. The detection of K_L is also important to reconstruct $B \rightarrow J/\Psi K_L$ modes which is interesting because of the CP eigenstate. Muons are identified as the charged track which penetrates iron plates.

The KLM consists of octagonal barrel region and two endcap regions. The angular coverage of KLM is $25^\circ < \theta < 145^\circ$. The structure of both region is a repetition of 47[mm] iron plates and 44[mm] Resistive Plate Counter (RPC) super-layer module. The barrel region has 15 layers and the endcap region has 14 layers. The barrel region has 240 RPC modules and the endcap region has 112 RPC modules.

An RPC is essentially a planer spark counters in which the avalanche induced by an incident charged particle is quenched when limited amount of charge on inner surface of highly resistive electrode is exhausted. the RPC is locally dead-end until the inner surfaces can re-charge through the resistive material (glass: $10^{12} \sim 10^{13}[\Omega \cdot \text{cm}]$). The RPC super-layer modules consists of two RPC layers of which the readout strip is orthogonal for each other. The width of readout strip is typically 5[cm].

The iron plate is energy absorber for K_L s through the strong interaction. On the other hand muons does not feel the strong interaction. The KLM separates K_L s from muons by catching the annihilation particles. The KLM measures the polar angle of K_L s with the 30[mrad] precision, but can not measure the momenta of muons.

2.4 Simulation software for the BELLE detector

2.4.1 Overview

The general framework of software and data flow for analysis is shown in Figure.2.8. All data transports, shown with arrows in Figure.2.8, are treated by a bank system called Panther which is developed for the BELLE. Monte Carlo simulation program consists of the QQ event generator and the GSIM detector simulation program. The detector simulator is based on GEANT and it simulates the behavior of particles in the detector and detector re-

sponses. The output format of the detector simulator is same as the experimental data format so that the same analysis program can be used for both MC and data samples. The reconstruction software calculate the momentum of the charged track and the energy of the photon. Particle identification of the charged track is also performed. Those results are stored in the Data Summary Table (DST). Individual physics analyses is performed using DST.

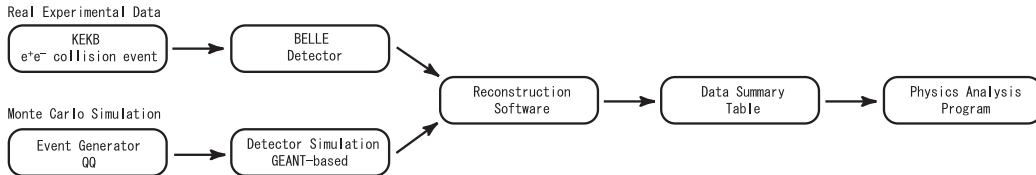


Figure 2.8: General Framework of Software

2.4.2 Event generator

We use the QQ event generator developed by CLEO to generate physics events of interest. It is designed to simulate the e^+e^- collision at the energy of $\Upsilon(4S)$. The QQ generates the primary particles such as $\Upsilon(4S)$, di-lepton and quark anti-quark pair ($u\bar{u}$, $d\bar{d}$, $s\bar{s}$, $c\bar{c}$) at the interaction point. The QQ make short lived particles decay according to the user-defined decay table and generate daughter particles.

The cross sections for various physics processes are shown in Table 2.1 at the energy of $\Upsilon(4S)$ mass. Although Bhabha and 2γ processes have larger cross sections than $\Upsilon(4S)$ production, these events are easily identified and rejected. In this analysis we only consider $\Upsilon(4S)$ and continuum events ($e^+e^- \rightarrow q\bar{q}$). $\Upsilon(4S)$ decays to $B^0\bar{B}^0$ and B^+B^- with a equal fraction. The QQ takes into account the spread of the interaction point (IP). The QQ also simulates the beam energy spread.

Physics Process	Cross Section [nb]
$\Upsilon(4S) \rightarrow BB$	1.15
Hadronic production from continuum	2.8
$\mu^+\mu^- + \tau^+\tau^-$	1.6
Bhabha	44
$\gamma\gamma$	2.4
2γ	~ 15

Table 2.1: Total cross section of e^+e^- collision at $\sqrt{s} = 10.58[\text{GeV}]$ for various processes.

2.4.3 Detector simulation

The particles generated by the QQ are fed into the GSIM detector simulator based on GEANT. The simulator takes into account the detailed configuration of all the BELLE sub-detectors. Particle interactions in the detector material, decay in flight and the bending of the trajectory in magnetic field are considered. For charged particle energy loss in the materials, the effect of fluctuation by δ -ray generation, the effect of multiple scattering, bremsstrahlung, positron annihilation are calculated using the standard formulas. The GSIM includes the photon conversion, Compton scattering, and photo-electric effect in the material. The interaction of hadron with the nucleus of the matter is also simulated. All particles propagate until they go out of the detector volume or their energies become lower than certain thresholds. The energy thresholds are 100[KeV] for a photon and an electron, 1[MeV] for a muon and a charged hadron, 10[MeV] for a neutral hadron. The GSIM generates the signal of each sub-detector from the calculated information of the interaction between particles and the detector material with smearing with the expected resolution.

2.4.4 Reconstruction software

The tracking software finds charged track trajectories from CDC wire hits and calculates the momentum from the trajectory, and then associates the charged track to corresponding SVD hits. The trajectory of a charged particle is helical in the magnetic field. Initially the track reconstruction software finds tracks in $r - \phi$ plane. The track is fitted by a helix function in 3 dimension with an assumption of uniform magnetic field. After the initial

fit, Kalman filtering (step by step χ^2 fit) method refit the tracks with realistic non-uniformed magnetic field. The efficiency to associate the reconstructed track from CDC with 2 or more SVD hits is 96% with the momentum higher than 500 [MeV/c]. The momentum resolution in the transverse to the beam direction P_t is measured to be $(0.25\pm 0.02)\%P_t\oplus(0.30\pm 0.004)\%$.

We use the Particle identification software developed at BELLE. The kaon identification software calculates the ratio of the kaon probability of certain track to the pion probability from CDC dE/dX , ACC, TOF information. The electron identification software calculates the electron probability of certain tracks from ECL and CDC dE/dX information. The muon identification software associates the charged track with KLM hits and identify muons based on the interaction depth the particle penetrates.

We use Kfitter[4] to obtain decay vertices of short-lived particles. Kfitter performs the vertex constraint fit with charged tracks and yields the common vertex position which gives minimum χ^2 . It re-calculates the momenta of the tracks with a constraint that the track should originate from the vertex.

Chapter 3

Lifetime measurement

3.1 Overview

The proper time difference Δt between two B decays is calculated from the distance of vertices of two B mesons as $\Delta t \simeq \Delta z / c\beta\gamma$. $\beta\gamma$ is the Lorentz boost factor due the asymmetric beam energy and 0.425 at KEKB. Δz is the distance between the two B decay vertices along the beam direction. Flight distance in xy plain is ignored because BB pair is produced almost at rest in the center-of-mass frame of the $\Upsilon(4S)$. Conceptual drawing of the Δz measurement is shown in figure.3.1. We reconstruct $B^0 \rightarrow D^{*-}\ell^+\nu$ and $B^+ \rightarrow \bar{D}^{*0}\ell^+\nu$ decay modes to separate daughter tracks of B meson from tracks of the other B meson. We select these modes because of large Branching ratio as shown Table. 3.1. D^* candidates are identified via $D^{*+} \rightarrow D^0\pi^+$, $D^{*0} \rightarrow D^0\pi^0$ decays¹ followed by $D^0 \rightarrow K^-\pi^+$, $D^0 \rightarrow K^-\pi^+\pi^0$ and $D^0 \rightarrow K^-\pi^+\pi^+\pi^-$ decay modes. Using same D^0 decay modes for both neutral and charged B meson reduces the difference between them. Because it is impossible to detect a neutrino, we select the $B \rightarrow D^*\ell\nu$ events with kinematical constraints from the combinations of the reconstructed D^* and the lepton with proper charge. We obtain the B decay vertices from the reconstructed D^* and lepton tracks with the vertex constraint fit[4]. The decay vertex of the other B , is obtained from the remaining charged tracks. Neutral and charged B meson lifetimes are derived by fitting the distribution of the proper time difference with a lifetime function convoluted by resolution function. In this chapter, we study selection of B candidates, proper time calculation and lifetime fit using a Monte Carlo Sample corresponding to $4[\text{fb}^{-1}]$. In this Monte Carlo Simulation, the input values of $c\tau$ are $468[\mu\text{m}]$

¹Charge conjugate mode are implied throughout this paper.

for B^0 and $486[\mu\text{m}]$ for B^+ .

Decay mode	BR
$B^+ \rightarrow \bar{D}^{*0} \ell^+ \nu_\ell$	$(5.3 \pm 0.8)\%$
$B^0 \rightarrow D^{*-} \ell^+ \nu_\ell$	$(4.60 \pm 0.27)\%$

Table 3.1: B^0 branching ratios to $D^* \ell \nu$.

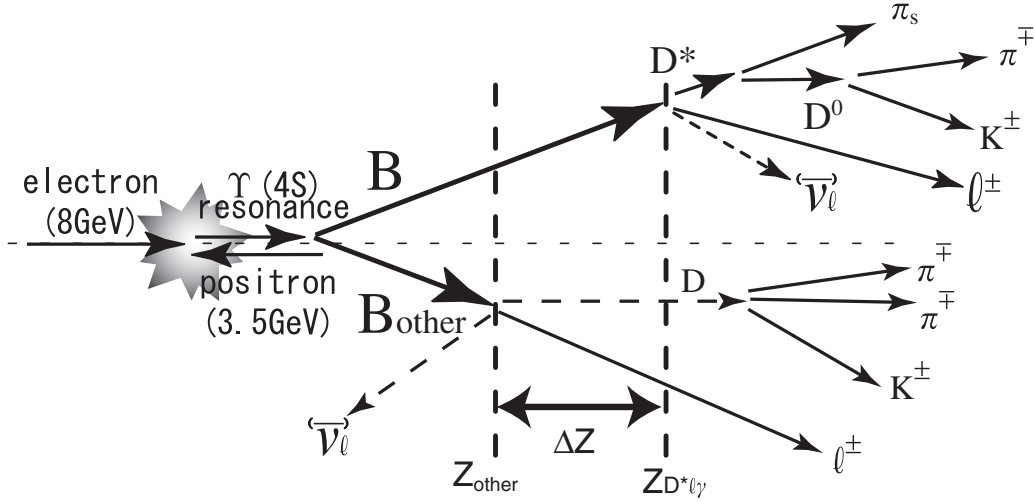


Figure 3.1: Conceptual drawing of the Δz measurement at KEKB.

3.2 Event reconstruction

3.2.1 Reconstruction of B meson

Reconstruction of D^0

D^0 mesons are reconstructed using $D^0 \rightarrow K^- \pi^+$, $D^0 \rightarrow K^- \pi^+ \pi^0$, $D^0 \rightarrow K^- \pi^+ \pi^+ \pi^-$ decay modes. Those decay modes are chosen because of the large branching ratios as listed in table.3.2 and smaller number of daughter particles.

All charged tracks are required to be associated with at least 2 SVD hits for the precise measurement of the vertex position. All charged tracks are required not to be included in the set of the daughter particles of K_S candidate. The charged D daughters are required to have particle identification from dE/dx , TOF and ACC consistent with the D daughter hypothesis, namely kaon and pion probability greater than 0.1 for kaon and pion tracks respectively. π^0 candidates are formed by 2 photons detected by the ECL and required to satisfy following conditions to reduce background. The χ^2 of mass constraint fit must be less than 5. Each daughter photons is required not to form another good π^0 candidate. The absolute value of the cosine of the angle between one of daughter photon and π^0 direction at the π^0 rest frame, $\cos\theta_{\pi^0\text{decay}}$, should be less than 0.9. The $\cos\theta_{\pi^0\text{decay}}$ distribution is flat for signal while it peaks at $\cos\theta_{\pi^0\text{decay}} = 1$ for background as shown fig.3.2. This cuts rejects 15% of background while retaining 94% of the signal.

The invariant mass distribution is shown in fig.3.3. The invariant mass of D^0 candidates must be within $1.8533 < M_{K\pi}[\text{GeV}] < 1.8793$ for $D^0 \rightarrow K^-\pi^+$ mode, $1.8439 < M_{K\pi\pi^0}[\text{GeV}] < 1.8808$ for $D^0 \rightarrow K^-\pi^+\pi^0$ mode and $1.8565 < M_{K\pi\pi\pi}[\text{GeV}] < 1.8772$ for $D^0 \rightarrow K^-\pi^+\pi^+\pi^-$ mode. This selection criteria is determined as $\pm 3\sigma$ of the invariant mass distribution except for $D^0 \rightarrow K^-\pi^+\pi^+\pi^-$ mode.²

Signal-to-background ratio of the $D^0 \rightarrow K^-\pi^+\pi^0$ mode can be improved by exploiting the resonance sub-structure in the final state. In addition to a non-resonant component, the $K^-\pi^+\pi^0$ final state is produced via the intermediate two body states; $K^-\rho^+$, $\bar{K}^{*0}\pi^0$ and $K^{*-}\pi^+$. The distribution of the signal, $S(x, y)$, across the Dalitz plot can be represented by

$$S(x, y) = \left| 1 + \sum_{k=1}^n c_k e^{i\theta} B_k(x, y) A_k(x, y) \right|^2 \quad (3.1)$$

where x and y are the squares of the masses of the two possible $K\pi$ combinations, c_k is the amplitude for the resonance k , θ_k is the phase angle, B_k is a normalized Breit-Wigner function and A_k describe the angular distributions. We use a routine written in CLEO Collaborations[3]. The S distributions for true and fake D^0 candidates are shown in Figure.3.4. A cut of $S > 20$ is imposed. This cuts rejects 51% of background while retaining 77% of the signal.

²The upper criteria of the invariant mass for $D^0 \rightarrow K^-\pi^+\pi^+\pi^-$ mode is determined as $+2.5\sigma$.

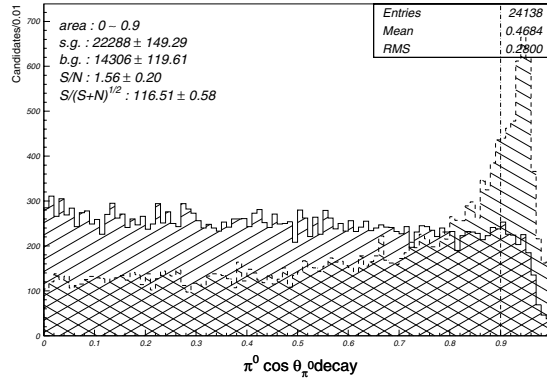
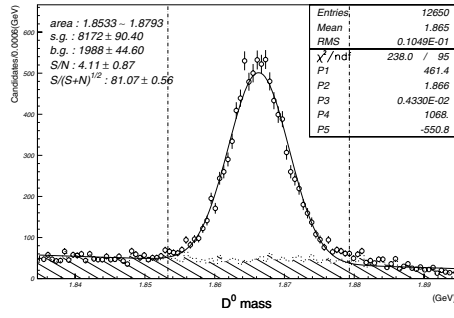


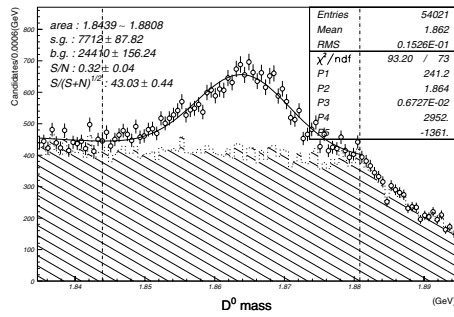
Figure 3.2: $\cos \theta_{\pi^0 \text{decay}}$ distribution for π^0 candidates. Solid line shows the distribution for the true π^0 . Dashed line shows the distribution for the fake π^0 . Selection criteria is indicated by dot-dashed line.

Decay mode	BR
$D^0 \rightarrow K^- \pi^+$	$(3.85 \pm 0.09)\%$
$D^0 \rightarrow K^- \pi^+ \pi^0$	$(13.9 \pm 0.9)\%$
$D^0 \rightarrow K^- \pi^+ \pi^+ \pi^-$	$(7.6 \pm 0.4)\%$

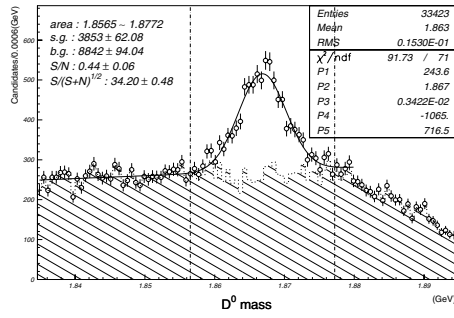
Table 3.2: D^0 branching ratios to decay modes of interest.



(a) $D^0 \rightarrow K^- \pi^+$



(b) $D^0 \rightarrow K^- \pi^+ \pi^0$



(c) $D^0 \rightarrow K^- \pi^+ \pi^+ \pi^-$

Figure 3.3: Invariant mass distribution for D^0 candidates. Solid line shows the the fit result with the sum of a Gaussian and a liner function. Dotted line shows the background distribution. Selection criteria is indicated by dot-dashed line.

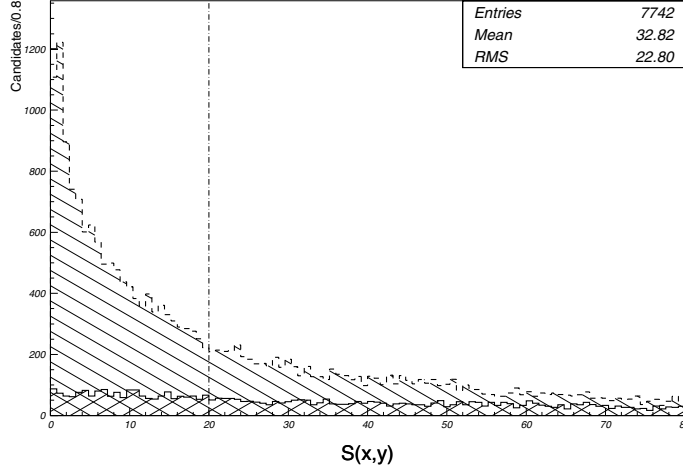


Figure 3.4: $S(x, y)$ distribution for $D^0 \rightarrow K\pi\pi^0$ candidates. Solid line shows the distribution for the true D^0 . Dashed line shows the distribution for the fake D^0 . Selection criteria is indicated by dot-dashed line.

Reconstruction of D^{*0} and D^{*+}

D^{*0} and D^{*+} are reconstructed using $D^{*0} \rightarrow D^0\pi^0$ and $D^{*+} \rightarrow D^0\pi^+$ decay mode respectively. Branching ratios of those decay modes are listed in table.3.3.

The shapes of the distributions of mass difference are represented by the sum of two Gaussians with a same mean for signal and a threshold function $\text{Th}(x; m^0, i, a^0, a^1, a^2)$ for background.

$$F(x = M_{D^*} - M_D) \propto \underbrace{G_2(x; g, \mu, \sigma_{\text{narrow}}, \sigma_{\text{wide}})}_{\text{signal fraction}} \quad (3.2)$$

$$+ \underbrace{\text{Th}(x; m^0, i, a^0, a^1, a^2)}_{\text{background fraction}} \quad (3.3)$$

$$G_2(x; g, \mu, \sigma_{\text{narrow}}, \sigma_{\text{wide}}) \equiv \frac{g}{\sqrt{2\pi}\sigma_{\text{narrow}}} \exp\left(-\frac{(x-\mu)^2}{2\sigma_{\text{narrow}}^2}\right) + \frac{1-g}{\sqrt{2\pi}\sigma_{\text{wide}}} \exp\left(-\frac{(x-\mu)^2}{2\sigma_{\text{wide}}^2}\right) \quad (3.4)$$

$$\text{Th}(x; m^0, i, a^0, a^1, a^2) \equiv (x - m^0)^i \exp(a^0 + a^1(x - m^0) + a^2(x - m^0)^2) \quad (3.5)$$

The distribution of the mass difference for each decay mode is shown in fig.3.6. The mass difference: $M_{D^*} - M_D$ of candidate must be within the regions listed on Table.3.4. This selection criteria is determined as $\pm 3\sigma_{\text{narrow}}$.³

Continuum event rejection

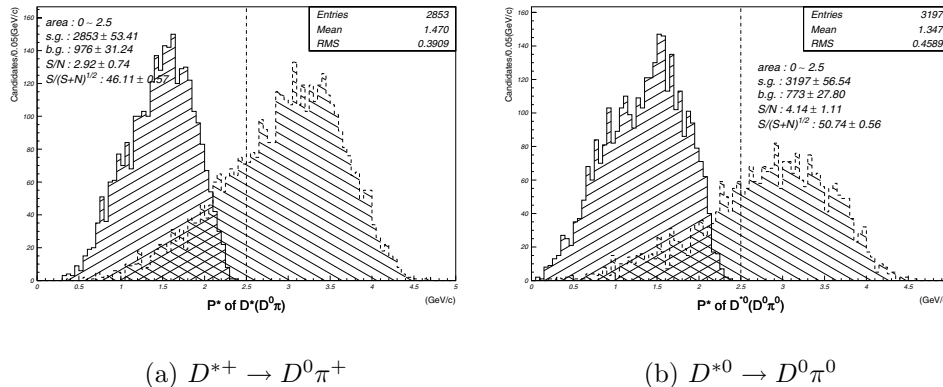


Figure 3.5: D^* momentum distribution. Solid lines show the distributions from $B \rightarrow D^* \ell \nu$ decays. Dashed lines show the distributions from the continuum background. Selection criteria are indicated by dot-dashed lines.

The D^* candidates are required to be in momentum range $p < 2.5$ [GeV/c] in $\Upsilon(4S)$ rest frame to reduce the D^* from the continuum background. The difference between D^* momentum distribution from $B \rightarrow D^* \ell \nu$ decay and from the continuum background is shown in Figure.3.5. This cuts rejects 63% of background while retaining 99% of the signal for $B^0 \rightarrow D^* \ell \nu$ decays and rejects 20% of background while retaining 99% of the signal for $B^+ \rightarrow D^{*0} \ell \nu$ decays .

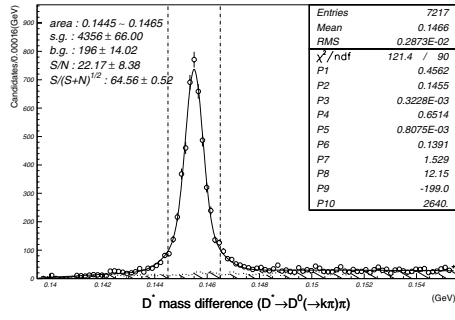
³The shape of signal distribution of $D^{*0} \rightarrow D^0(K^- \pi^+ \pi^+ \pi^-) \pi^0$ mode is similar to a single Gaussian rather than the sum of two Gaussians with a same mean. We perform a fit with the sum of single gaussian and the threshold function $\text{Th}(x)$ and determine the selection criteria as $\pm 3\sigma$ of gaussian.

Decay mode	BR
$D^{*0} \rightarrow D^0 \pi^0$	$(61.9 \pm 2.9)\%$
$D^{*+} \rightarrow D^0 \pi^+$	$(68.3 \pm 1.4)\%$

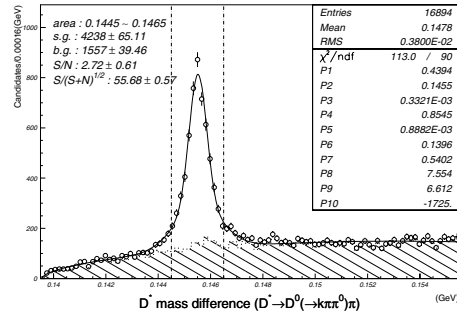
Table 3.3: D^{*0} and D^{*+} branching ratios to decay modes of interest.

$D^{*+} \rightarrow D^0(\rightarrow K^- \pi^+) \pi^+$	$0.1445 < M(D^{*+}) - M(D^0)[\text{GeV}] < 0.1465$
$D^{*+} \rightarrow D^0(\rightarrow K^- \pi^+ \pi^0) \pi^+$	$0.1445 < M(D^{*+}) - M(D^0)[\text{GeV}] < 0.1465$
$D^{*+} \rightarrow D^0(\rightarrow K^- \pi^+ \pi^+ \pi^-) \pi^+$	$0.1443 < M(D^{*+}) - M(D^0)[\text{GeV}] < 0.1466$
$D^{*0} \rightarrow D^0(\rightarrow K^- \pi^+) \pi^0$	$0.1407 < M(D^{*0}) - M(D^0)[\text{GeV}] < 0.1435$
$D^{*0} \rightarrow D^0(\rightarrow K^- \pi^+ \pi^0) \pi^0$	$0.1408 < M(D^{*0}) - M(D^0)[\text{GeV}] < 0.1434$
$D^{*0} \rightarrow D^0(\rightarrow K^- \pi^+ \pi^+ \pi^-) \pi^0$	$0.1406 < M(D^{*0}) - M(D^0)[\text{GeV}] < 0.1434$

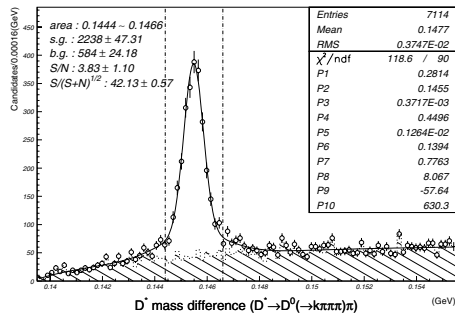
Table 3.4: The mass difference criteria of D^{*+} and D^{*0}



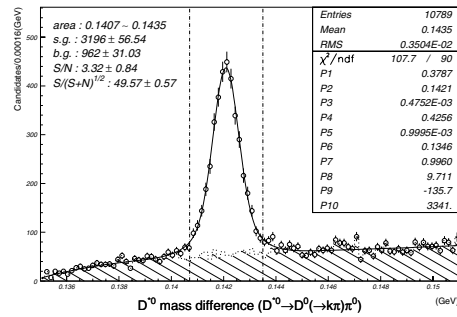
(a) $D^{*+} \rightarrow D^0(K^- \pi^+) \pi^+$



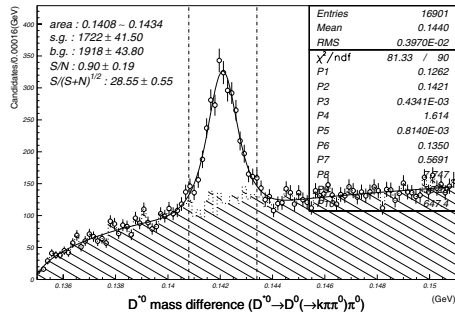
(b) $D^{*+} \rightarrow D^0(K^- \pi^+ \pi^0) \pi^+$



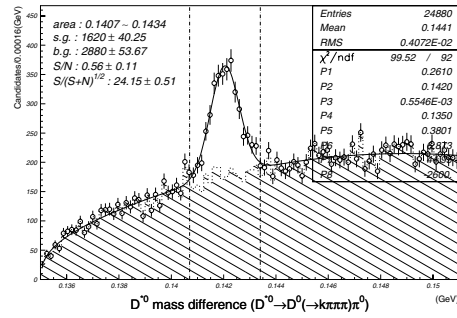
(c) $D^{*+} \rightarrow D^0(K^- \pi^+ \pi^+ \pi^-) \pi^+$



(d) $D^{*0} \rightarrow D^0(K^- \pi^+) \pi^0$



(e) $D^{*0} \rightarrow D^0(K^- \pi^+ \pi^0) \pi^0$



(f) $D^{*0} \rightarrow D^0(K^- \pi^+ \pi^+ \pi^-) \pi^0$

Figure 3.6: The mass difference distribution of D^{*0} and D^{*+} candidates. Solid line shows the results of the fit with the Eq.3.2. Dotted line shows the distribution of background. Selection criteria is indicated by dot-dashed line.

Association of D^* and lepton

Electrons are identified using dE/dx , the shape of the shower in the ECL and $E/|\mathbf{p}|$, the ratio of the candidate's energy deposit in the ECL to its momentum measured by the CDC. Muons identified by the KLM must not be positively identified as kaon. A lepton with the highest momentum in the $\Upsilon(4S)$ rest frame in the event is chosen and its momentum must be within $1.0 < P_{\text{lepton}}^*[\text{GeV}/c] < 2.5$ for B^0 and within $1.2 < P_{\text{lepton}}^*[\text{GeV}/c] < 2.5$ for B^+ . The lepton momentum distributions for signal and background are shown in Figure.3.8. This cuts rejects 54% of background while retaining 95% of the signal for $B^0 \rightarrow D^*\ell\nu$ decays and rejects 68% of background while retaining 52% of the signal for $B^+ \rightarrow D^{*0}\ell\nu$ decays .

Because it is impossible to detect a neutrino, we select $B \rightarrow D^*\ell\nu$ candidates with kinematical constraints from the combinations of the reconstructed D^* and the lepton with proper charge. In the $B \rightarrow D^*\ell\nu$ decay neutrino mass can be expressed as;

$$m_\nu^2 = (E_B - (E_{D^*} + E_\ell))^2 - (\mathbf{p}_{D^*} + \mathbf{p}_\ell)^2 - \mathbf{p}_B^2 + 2|\mathbf{p}_B| \cdot |\mathbf{p}_{D^*} + \mathbf{p}_\ell| \cos \theta_{B-D^*\ell}.$$

Definition of parameters are shown in Figure.3.7. All parameters are known or measured except $\cos \theta_{B-D^*\ell}$. Since the B momentum is sufficiently small ($\simeq 0.3[\text{GeV}]$) compared to the typical values of $|\mathbf{p}_\ell|$ and $|\mathbf{p}_{D^*}|$, we define missing mass squared MM^2 as;

$$MM^2 \equiv (E_B - (E_{D^*} + E_\ell))^2 - (\mathbf{p}_{D^*} + \mathbf{p}_\ell)^2$$

by assuming $\mathbf{p}_B = 0$.

The $|MM^2|$ distributions for signal and background are shown in Figure.3.9. The candidates are required to be within $|MM^2| < 1.35 [\text{GeV}^2]$. This cuts rejects 33% of background while retaining 94% of the signal for $B^0 \rightarrow D^*\ell\nu$ decays and rejects 31% of background while retaining 99% of the signal for $B^+ \rightarrow D^{*0}\ell\nu$ decays .

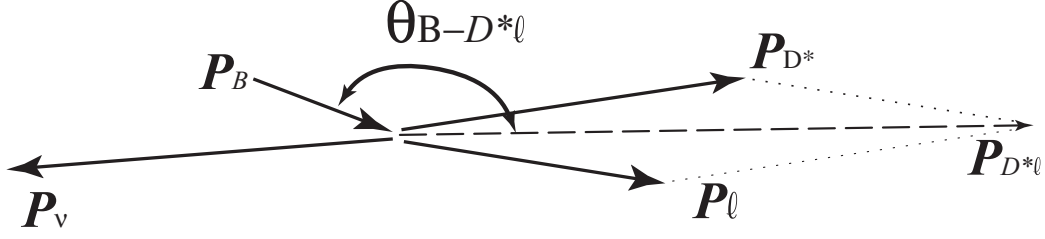


Figure 3.7: Parameters in $B \rightarrow D^* \ell \nu$

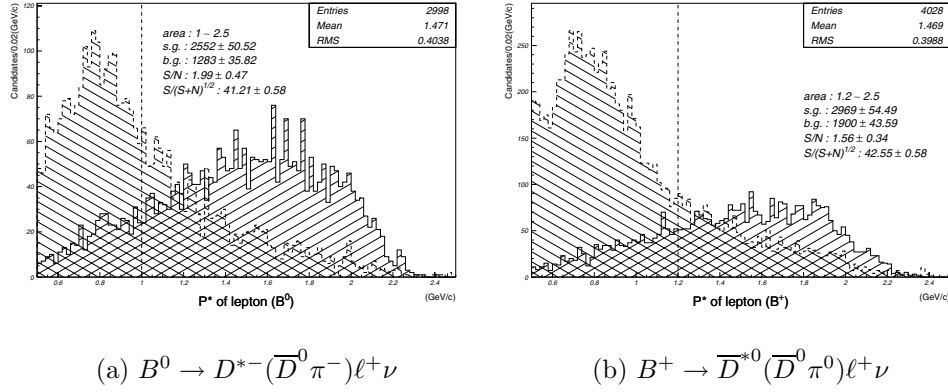
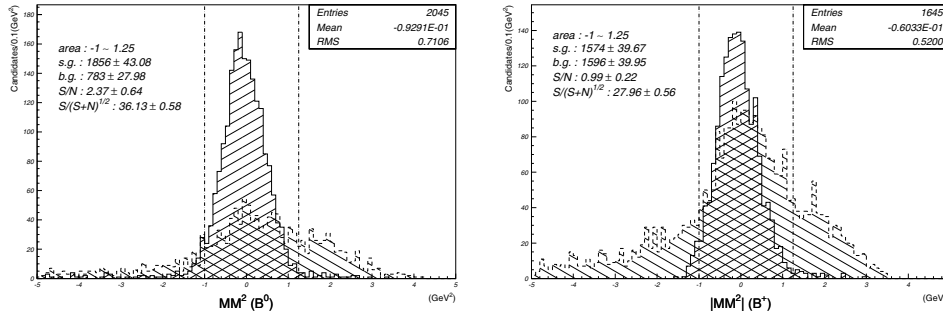


Figure 3.8: The lepton momenta distribution of B^0 and B^+ candidates in $\Upsilon(4S)$ rest frame. Solid line shows the values of the leptons from $B \rightarrow D^* \ell \nu$ decays. Dashed line shows the values of the fake leptons and the true lepton from the other reaction. Selection criteria are indicated by dot-dashed lines.



(a) $B^0 \rightarrow D^{*-}(\overline{D}^0 \pi^-)\ell^+\nu$

(b) $B^+ \rightarrow \overline{D}^{*0}(\overline{D}^0 \pi^0)\ell^+\nu$

Figure 3.9: The $|MM^2|$ distribution of B^0 and B^+ candidates. Solid line shows the values of the true $B \rightarrow D^*\ell\nu$ events. Dashed line shows the values of the wrong combination of D^* and ℓ . Selection criteria are indicated by dot-dashed lines.

3.3 Vertex reconstruction

The decay vertex of $B \rightarrow D^*\ell\nu$ is obtained with the vertex constraint fit with “IP (interaction point) constraint” using the lepton track and the reconstructed D^0 track. “IP constraint” requires the vertex to be within the the B decay region around the IP in a vertex constraint fit. The B decay region around the IP is smeared by a finite B flight length of $20 \mu\text{m}$ in xy-plane. A typical IP size is $\sigma_x = 80[\mu\text{m}]$, $\sigma_y = 4[\mu\text{m}]$, $\sigma_z = 3[\text{mm}]$. The IP position and σ_z are measured for each run using data. There is no inefficiency due to the vertex fit. To obtain the distance between two B decays (Δz), we compute the vertex of the associated B decay using remaining charged tracks. We require that the charged tracks to be associated with at least 2 SVD hits and not to be included in the set of the daughter particles of K_S candidate for the precise measurement of the vertex position. The efficiency to find the vertex position of the associated B decay is 94%. This method cause a systematic shift of the vertex position since it does (can) not distinguish D decay daughters from B decay daughters. The D decay point is shifted forward due to finite D lifetimes.

Figure.3.10 shows the distributions of $\Delta z_{\text{reconstructed}} - \Delta z_{\text{generated}}$. This corresponds to the Δz resolution. The distribution is fitted with the sum of

two Gaussians to account for its long tail. The fit results are superimposed on the distributions of the $\Delta z_{\text{reconstructed}} - \Delta z_{\text{generated}}$ in Figure.3.10. We obtain the parameters of Gaussians as follows.

$$(\Delta z_{\text{reconstructed}} - \Delta z_{\text{generated}}) \propto \left\{ \frac{g}{\sqrt{2\pi}\sigma_1} \exp\left(-\frac{(\Delta Z - \mu_1)^2}{2\sigma_1^2}\right) + \frac{1-g}{\sqrt{2\pi}\sigma_2} \exp\left(-\frac{(\Delta Z - \mu_2)^2}{2\sigma_2^2}\right) \right\}$$

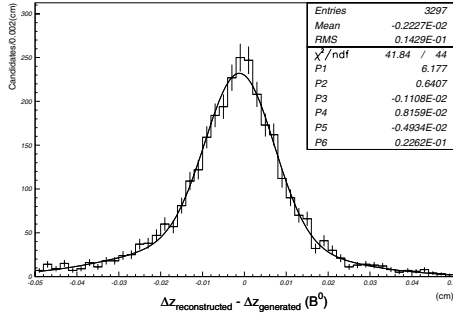
For $B^0 \rightarrow D^* \ell \nu$

$$\begin{aligned} g &= 0.65 \pm 0.04 \\ \mu_1 &= -11 \pm 3 \text{ } [\mu\text{m}] \\ \sigma_1 &= 82 \pm 4 \text{ } [\mu\text{m}] \\ \mu_2 &= -51 \pm 10 \text{ } [\mu\text{m}] \\ \sigma_2 &= 227 \pm 17 \text{ } [\mu\text{m}] \end{aligned}$$

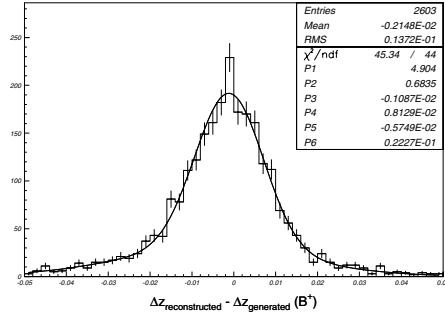
For $B^+ \rightarrow D^{*0} \ell \nu$

$$\begin{aligned} g &= 0.69 \pm 0.04 \\ \mu_1 &= -11 \pm 3 \text{ } [\mu\text{m}] \\ \sigma_1 &= 82 \pm 3 \text{ } [\mu\text{m}] \\ \mu_2 &= -59 \pm 12 \text{ } [\mu\text{m}] \\ \sigma_2 &= 224 \pm 18 \text{ } [\mu\text{m}] \end{aligned}$$

We also study the Δz resolution for different D^0 reconstruction modes to confirm that the resolution is independent of the D^0 reconstruction modes. Figure.3.11 shows the distribution of the $(\Delta z_{\text{reconstructed}} - \Delta z_{\text{generated}})$ for each D^0 reconstruction modes. The shapes of resolution function are similar because the Δz resolution is dominated by the vertex resolution of the associated B decay.

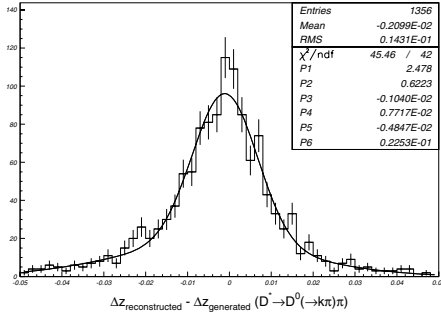


(a) $B^0 \rightarrow D^{*-}(\bar{D}^0 \pi^-)\ell^+\nu$

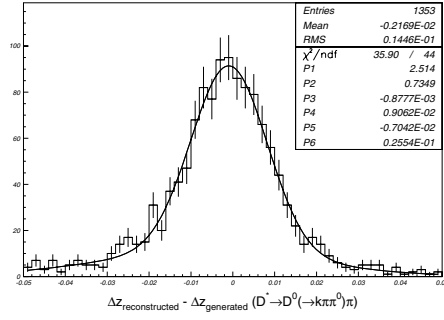


(b) $B^+ \rightarrow \bar{D}^{*0}(\bar{D}^0 \pi^0)\ell^+\nu$

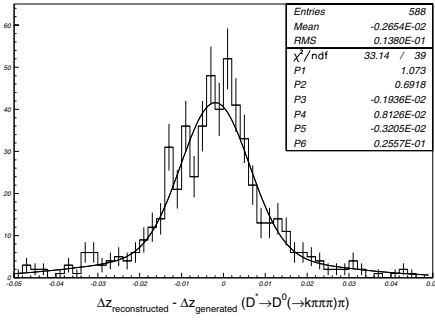
Figure 3.10: Distributions of $(\Delta z_{\text{reconstructed}} - \Delta z_{\text{generated}})$ for $B^0 \rightarrow D^*\ell\nu$ (a) and $B^+ \rightarrow D^{*0}\ell\nu$ (b). Fit results with the sum of two Gaussians are indicated by solid curves.



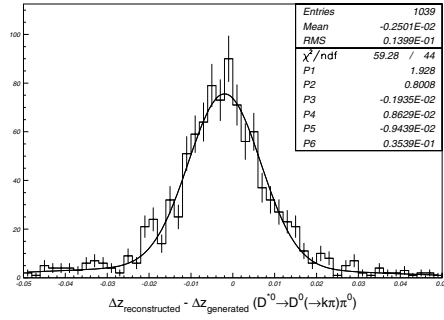
(a) $B^0 \rightarrow D^{*-}(\bar{D}^0(K^+\pi^-\pi^-\pi^0))\ell^+\nu$



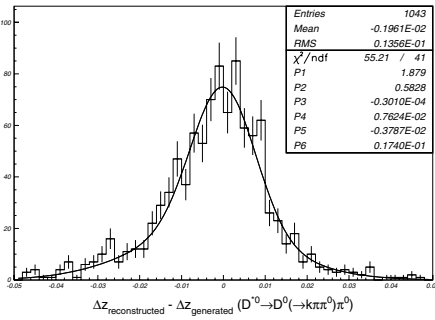
(b) $B^0 \rightarrow D^{*-}(\bar{D}^0(K^+\pi^-\pi^0)\pi^-\pi^0)\ell^+\nu$



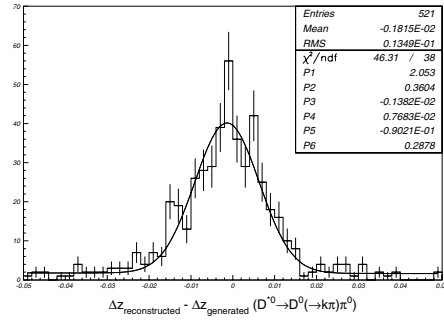
(c) $B^0 \rightarrow D^{*-}(\bar{D}^0(K^+\pi^+\pi^-\pi^-\pi^-\pi^0))\ell^+\nu$



(d) $B^+ \rightarrow \bar{D}^{*0}(\bar{D}^0(K^+\pi^-\pi^0))\ell^+\nu$



(e) $B^+ \rightarrow \bar{D}^{*0}(\bar{D}^0(K^+\pi^-\pi^0)\pi^0)\ell^+\nu$



(f) $B^+ \rightarrow \bar{D}^{*0}(\bar{D}^0(K^+\pi^+\pi^-\pi^-\pi^0))\ell^+\nu$

Figure 3.11: The distribution of the $(\Delta z_{\text{reconstructed}} - \Delta z_{\text{generated}})$ for different D^0 decay modes. Fit results with the sum of two Gaussians are indicated by solid curves.

3.4 Lifetime fit to signal

B meson lifetimes are extracted from the distribution of the proper time difference Δt of two B decays with an unbinned maximum likelihood fit. The ideal distribution of the proper time difference is represented by Eq.3.6 with the B meson lifetime: τ_B .

$$F_{\text{ideal}}(\Delta t) = \frac{1}{2\tau_B} \exp\left(-\frac{|\Delta t|}{\tau_B}\right) \quad (3.6)$$

In reality, the proper time distribution is smeared by the detector resolution. The realistic proper time distribution is the convolution of the ideal one with the resolution function \mathcal{R} .

$$\begin{aligned} F_{\text{real}}(\Delta t) &= F_{\text{ideal}}(\Delta t) \otimes \mathcal{R}(\Delta t) \\ &= \int_{-\infty}^{\infty} dt' \frac{1}{2\tau_B} \exp\left(-\frac{|t'|}{\tau_B}\right) \mathcal{R}(\Delta t, t') \end{aligned} \quad (3.7)$$

The shape of the resolution function is assumed as the sum of two Gaussians as discussed in Section.3.3.

We perform a lifetime fit to the signal events separated from fake events using the Monte Carlo generation information to evaluate the fit procedure. The likelihood function for the signal events expressed as;

$$\begin{aligned} \mathcal{L}(\tau_B, g, \mu_1, \sigma_1, \mu_2, \sigma_2) &= \prod_i \mathcal{L}_{\text{sig}}^i(\Delta z_i; \tau_B, g, \mu_1, \sigma_1, \mu_2, \sigma_2) \\ \mathcal{L}_{\text{sig}}^i(\Delta z; \tau_B, g, \mu_1, \sigma_1, \mu_2, \sigma_2) &= \frac{1}{2c\tau_B\beta\gamma} \exp\left(-\frac{|\Delta z|}{c\tau_B\beta\gamma}\right) \otimes \mathcal{R}(\Delta z; g, \mu_1, \sigma_1, \mu_2, \sigma_2) \\ \mathcal{R}(\Delta z; g, \mu_1, \sigma_1, \mu_2, \sigma_2) &= \left\{ \frac{g}{\sqrt{2\pi}\sigma_1} \exp\left(-\frac{(\Delta z - \mu_1)^2}{2\sigma_1^2}\right) \right. \\ &\quad \left. + \frac{1-g}{\sqrt{2\pi}\sigma_2} \exp\left(-\frac{(\Delta z - \mu_2)^2}{2\sigma_2^2}\right) \right\} \end{aligned}$$

where the product represented by index i is over the true signal events. We minimize a $-2\log\mathcal{L}$ in the fit. The extracted lifetimes of $c\tau = 482 \pm 57[\mu\text{ m}]$ for B^0 and $c\tau = 359 \pm 77[\mu\text{ m}]$ for B^+ are consistent with the input values of $c\tau = 468[\mu\text{ m}]$ for B^0 and $c\tau = 486[\mu\text{ m}]$, respectively. The parameters for the resolution function are also consistent with those obtained in the previous section. The Δz distribution with fits are shown in Figure.3.12.

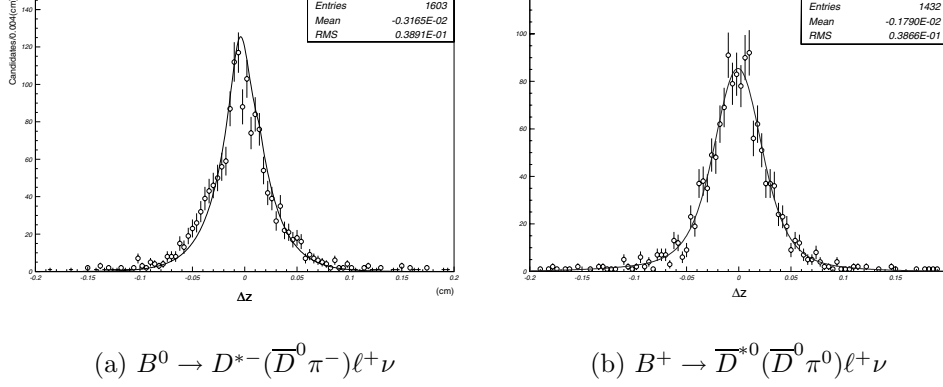


Figure 3.12: The Δz distribution for signal. The points represent the reconstructed Δz . Solid lines represent the fit results.

3.5 Background estimation

Likelihood function for background is studied. The background from continuum events is expected to have zero lifetime since all tracks come from the interaction point while the background in the $B\bar{B}$ events is expected to have a finite lifetime. Taking these into account the likelihood function for the backgrounds are defined as;

$$\begin{aligned}
 & \mathcal{L}(\tau_{bkg}, f_{bkg}^0, g, \mu_1, \sigma_1, \mu_2, \sigma_2) \\
 &= \prod_j \mathcal{L}_{bkg}^j(\Delta z_i) \\
 \mathcal{L}_{bkg}^j(\Delta z) &= \left\{ f_{bkg}^0 \delta(\Delta z) + (1 - f_{bkg}^0) \frac{1}{2c\tau_{bkg}\beta\gamma} \exp\left(-\frac{|\Delta z|}{c\tau_{bkg}\beta\gamma}\right) \right\} \otimes \mathcal{R}(\Delta z) \\
 \mathcal{R}(\Delta z; g, \mu_1, \sigma_1, \mu_2, \sigma_2) &= \frac{g}{\sqrt{2\pi}\sigma_1} \exp\left(-\frac{(\Delta z - \mu_1)^2}{2\sigma_1^2}\right) + \frac{(1-g)}{\sqrt{2\pi}\sigma_2} \exp\left(-\frac{(\Delta z - \mu_2)^2}{2\sigma_2^2}\right)
 \end{aligned}$$

where the product represented by index j is over the sample events of background. The lifetime fit is performed using this likelihood function for the background sample in the upper sideband region of the missing mass squared distribution. The results of the lifetime fits for B^0 and B^+ are shown in Figure.3.13. Fit represents the Δz distribution well confirming the validity of

the likelihood function. The parameters obtained by the fits are summarized in Table.3.5.

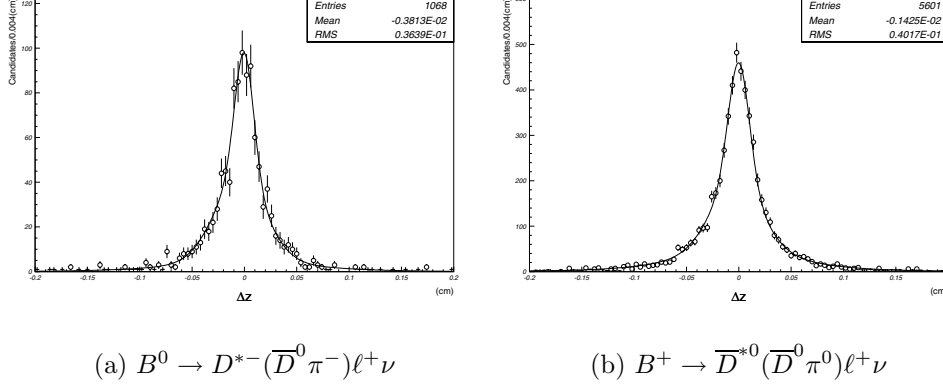


Figure 3.13: Δz distributions in the MM^2 sidebands. Solid lines show the fit results.

mode	$c\tau_{bkg}$ [μ m]	f_{bkg}^0
$B^0 \rightarrow D^{*-} \ell^+ \nu$	1111 ± 161	0.765 ± 0.061
$B^+ \rightarrow \overline{D}^{*0} \ell^+ \nu$	1033 ± 55	0.609 ± 0.040

Table 3.5: Results of the lifetime fit for the background (MM^2 sidebands).

A fraction of the signal in the signal region is estimated from the distribution of the missing mass squared. The MM^2 distribution is fitted with a Gaussian $G(x; A_{sig}, \mu_{sig}, \sigma_{sig})$ for the signal and a 9th order polynomial $P_9(x; \{a_{bg}^i\})$. Figure3.9 show the missing mass squared distribution with the fit. The signal probability $p_{\ell-D^*sig}$ for a given MM^2 (Fig.3.14) can be expressed as;

$$p_{\ell-D^*sig}(|MM^2|) = G(MM^2)/(G(MM^2) + P_9(MM^2)).$$

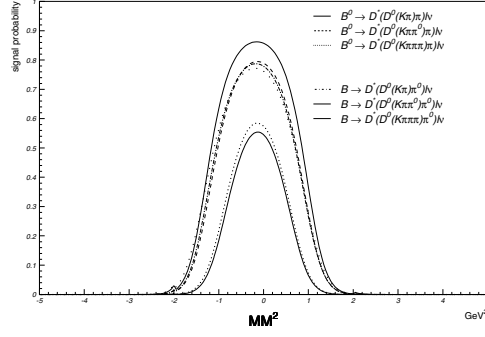


Figure 3.14: Signal probability

3.6 Lifetime fit with background

Combining likelyhood functions for the signal and the background, the likelyhood function is defined as;

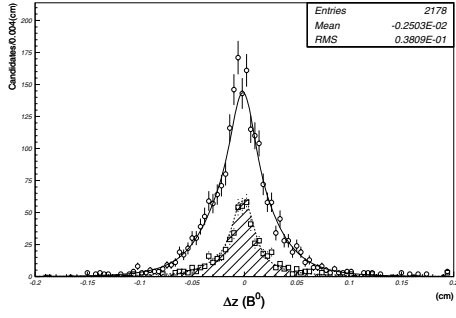
$$\begin{aligned}
& \mathcal{L}(\tau_B, \tau_{bg}, f_{bg}^0, g, \mu_1, \sigma_1, \mu_2, \sigma_2) \\
&= \left[\prod_i \{ p_{sig}^i \mathcal{L}_{sig}^i(\Delta z_i) + (1 - p_{sig}^i) \mathcal{L}_{bg}^i(\Delta z_i) \} \right] \\
\mathcal{L}_{sig}^i(\Delta z) &= \frac{1}{2c\tau_B\beta\gamma} \exp\left(-\frac{|\Delta z|}{c\tau_B\beta\gamma}\right) \otimes \mathcal{R}(\Delta z) \\
\mathcal{L}_{bg}^i(\Delta z) &= \left\{ f_{bg}^0 \delta(\Delta z) + (1 - f_{bg}^0) \frac{1}{2c\tau_{bg}\beta\gamma} \exp\left(-\frac{|\Delta z|}{c\tau_{bg}\beta\gamma}\right) \right\} \otimes \mathcal{R}(\Delta z) \\
& \mathcal{R}(\Delta z; g, \mu_1, \sigma_1, \mu_2, \sigma_2) \\
&= \frac{g}{\sqrt{2\pi}\sigma_1} \exp\left(-\frac{(\Delta z - \mu_1)^2}{2\sigma_1^2}\right) + \frac{(1 - g)}{\sqrt{2\pi}\sigma_2} \exp\left(-\frac{(\Delta z - \mu_2)^2}{2\sigma_2^2}\right)
\end{aligned}$$

where the product represented by index i is over the $B \rightarrow D^* \ell \nu$ candidates. p_{sig}^i is a signal probability of each candidate and it is derived from the MM^2 distribution as discussed in the previous section. Candidates in the MM^2 sideband region are also included in the fit to obtain fit parameters associated with the background simultaneously. The fits yields;

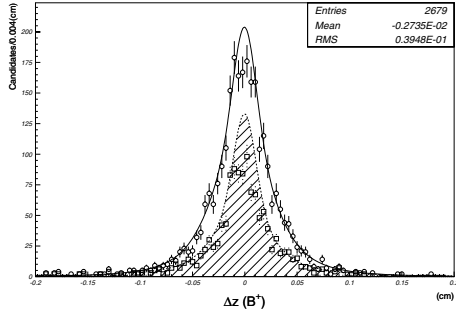
$$\begin{aligned}
c\tau_{B^0} &= 521 \pm 26 [\mu\text{m}] \\
(\tau_{B^0} &= 1.74 \pm 0.087 [\text{ps}])
\end{aligned}$$

$$\begin{aligned}c\tau_{B^+} &= 477 \pm 30[\mu\text{m}] \\(\tau_{B^+} &= 1.50 \pm 0.10[\text{ps}])\end{aligned}$$

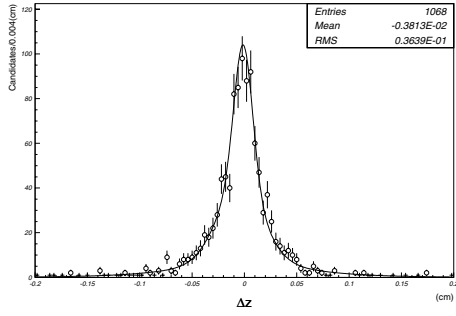
The input values of $c\tau$ are $468[\mu\text{m}]$ ($1.56[\text{ps}]$) for B^0 and $486[\mu\text{m}]$ ($1.62[\text{ps}]$) for B^+ . The fits give consistent results with the input values. Parameters of the resolution function from the lifetime fits are compared with the results from the direct measurement in section 3.3 as shown in Table 3.6. They agree with each other. Parameters for the background function in the fit are also compared with the results in Sec 3.5 as shown in Table 3.7. They are consistent.



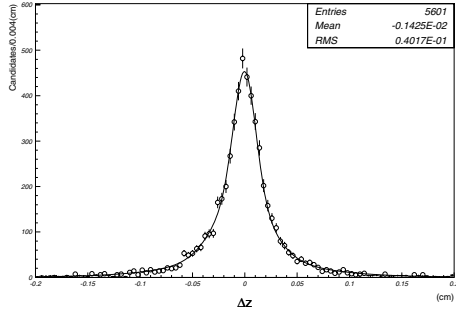
(a) $B^0 \rightarrow D^{*-}(\overline{D}^0 \pi^-)\ell^+\nu MM^2$ signal region



(b) $B^+ \rightarrow \overline{D}^{*0}(\overline{D}^0 \pi^0)\ell^+\nu MM^2$ signal region



(c) $B^0 \rightarrow D^{*-}(\overline{D}^0 \pi^-)\ell^+\nu MM^2$ side-band region



(d) $B^+ \rightarrow \overline{D}^{*0}(\overline{D}^0 \pi^0)\ell^+\nu MM^2$ side-band region

Figure 3.15: Circle points show Decay length difference distributions. Square points in (a) and (b) show background distribution. Solid lines show results of lifetime fits. Dotted lines in (a) and (b) show the background components of the results

mode	g	μ_1 [μ m]	σ_1 [μ m]	μ_2 [μ m]	σ_2 [μ m]
$B^0 \rightarrow D^{*-}\ell^+\nu$	0.470 ± 0.099	-11 ± 8	88 ± 11	-44 ± 14	210 ± 23
	0.645 ± 0.038	-11 ± 3	82 ± 4	-51 ± 10	227 ± 17
$B^+ \rightarrow \overline{D}^{*0}\ell^+\nu$	0.497 ± 0.073	-1 ± 5	103 ± 8	-30 ± 10	235 ± 20
	0.689 ± 0.037	-11 ± 3	82 ± 3	-59 ± 12	224 ± 18

Table 3.6: The resolutions derived from the lifetime fit(above) and the resolutions derived from the generator information (below)

mode	f_{bg}^0	$c\tau_{bg}$ [μ m]
$B^0 \rightarrow D^{*-}\ell^+\nu$	0.694 ± 0.054	1067 ± 110
	0.765 ± 0.061	1111 ± 161
$B^+ \rightarrow \overline{D}^{*0}\ell^+\nu$	0.608 ± 0.036	1048 ± 51
	0.608 ± 0.400	1032 ± 55

Table 3.7: The background parameters derived from the lifetime fit(above) and the background parameters derived from the fit with background samples(below)

Chapter 4

Data Analysis

We analyze $0.2 \text{ [fb}^{-1}\text{]}$ of experimental data taken with the BELLE detector from July.1999 to Dec.1999. We do not use any input from the MC sample for the data analysis. We analyze the data with hadronic event selection shown in Table4.1. Due to the difference in the detector resolution between the data and MC the mass difference of D^* candidate must be within $0.1435 < M(D^{*+}) - M(D^0)[\text{GeV}] < 0.1474$ for D^{*+} and $0.1400 < M(D^{*0}) - M(D^0)[\text{GeV}] < 0.1440$ for D^{*0} . Figures 4.1(a) and 4.1(a) show the Δm distributions with fits by the sum of two Gaussian plus a threshold function for D^{*+} and D^{*0} respectively. Since we can not find any significant peak in the mass difference with $D^{*0} \rightarrow D^0\pi^0$, $D^0 \rightarrow K^-\pi^+\pi^+\pi^-$ mode this mode is excluded from the data analysis. The other selection criteria are same as the Monte Carlo study. Single Gaussian is used for the resolution function in the lifetime fit instead of the sum of two Gaussians because statistics is small. The B^0 lifetime is measured to be;

$$\begin{aligned} c\tau_{B^0} &= 593 \pm 130[\mu\text{m}] \\ \tau_{B^0} &= 1.98 \pm 0.43[\text{ps}]. \end{aligned}$$

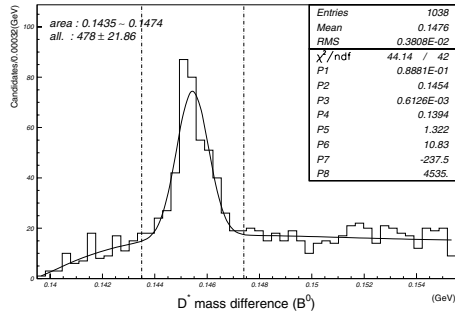
The current world average value is

$$\begin{aligned} c\tau_{B^0} &= 468 \pm 12[\mu\text{m}] \\ \tau_{B^0} &= 1.56 \pm 0.04[\text{ps}]. \end{aligned}$$

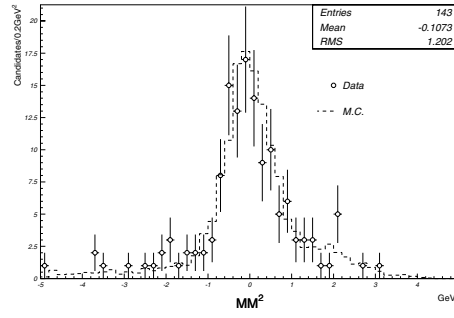
The other parameters derived from fit are shown in Table.4.2. We cannot obtain meaningful results from the B^+ candidates due to poor statistics at the present time. Figures 4.1(b),(c) and 4.1(b),(c) show the Δz distributions with the results of the lifetime fits for B^0 and B^+ and in the MM^2 signal and sideband regions, respectively. The fits represent the distribution well for both signal and background regions.

The number of charged tracks with good quality	≥ 5
The radial component of primary vertex	$< 1.5[\text{cm}]$
The absolute value of the z component of primary vertex	$< 3.5[\text{cm}]$
The ratio of Total visible energy to the center-of-mass energy	$\geq 50\%$
The ratio of absolute value of z component sum for charged track momentum and clusters energy in the $\Upsilon(4S)$ rest frame to the center-of-mass energy	$\leq 30\%$
The ratio of the sum of the energy deposit in ECL to the center-of-mass energy $E_{\text{ECL}}/E_{\text{CM}}$	$2.5\% \leq E_{\text{ECL}}/E_{\text{CM}} \leq 90\%$.

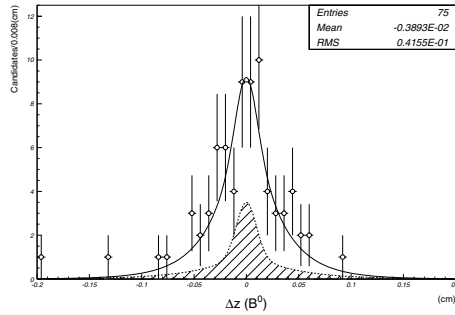
Table 4.1: The selection criteria of hadronic event selection



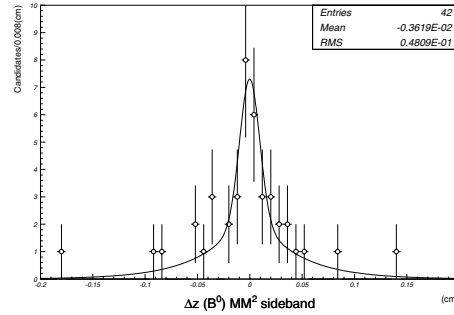
(a) D^* mass difference distribution



(b) The MM^2 distribution



(c) The decay length distribution and the result of lifetime fit for MM^2 signal region.

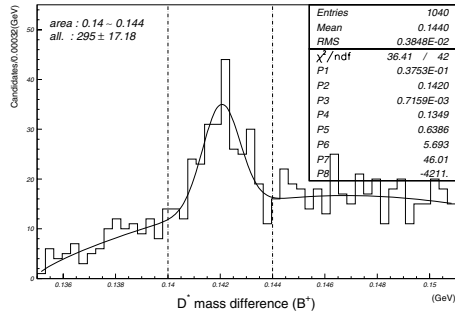


(d) The decay length distribution and the result of lifetime fit for MM^2 sideband region.

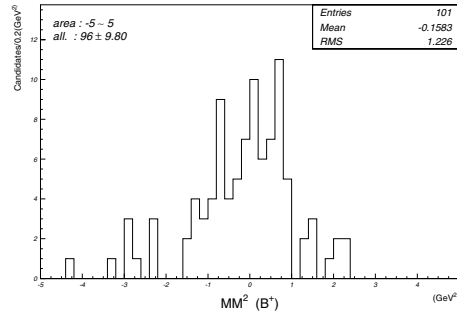
Figure 4.1: The result of reconstruction and life time fit of neutral B meson

μ of \mathcal{R} [μm]	σ of \mathcal{R} [μm]	f_{bg}^0	$c\tau_{bg}$ [μm]
0 ± 24	94 ± 45	0.361 ± 0.190	974 ± 280

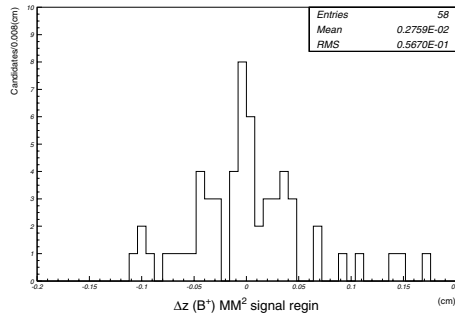
Table 4.2: Obtained parameters of lifetime fit



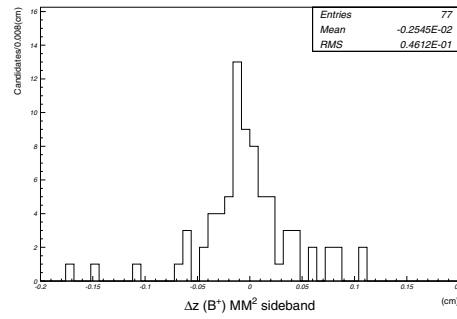
(a) D^* mass difference distribution



(b) The MM^2 distribution



(c) The decay length distribution and the result of lifetime fit for MM^2 signal region.



(d) The decay length distribution and the result of lifetime fit for MM^2 sideband region.

Figure 4.2: The result of reconstruction and life time fit of charged B meson

Chapter 5

Conclusions

The KEK B factory has advantages for the measurement of B meson lifetimes in several points. We can reduce the statistical error in the lifetime measurement because a large amount of B mesons is provided by accelerator with small background.

Selection of B candidates, calculation of the proper-time difference, extraction of the lifetime from the fit are studied using the Monte Carlo samples corresponding to $4[\text{fb}^{-1}]$. The lifetime fit is demonstrated to yield correct lifetime from the proper-time distribution.

The lifetime measurement is also very useful to understand the performance of the BELLE detector. It is crucial to understand the Δz resolution function for the CP violation measurement which is one of the most important goal of the B factory experiment. It is also demonstrated that we can obtain the resolution function of the Δz as the result of the lifetime fit.

We measure B^0 lifetime based on the $0.2[\text{fb}^{-1}]$ of data collected with the BELLE. The B^0 lifetime is measured to be $c\tau_{B^0} = 593 \pm 130[\mu\text{m}]$ ($\tau_{B^0} = 1.98 \pm 0.48[\text{ps}]$.)

Appendix A

Remaining problems and future plans

There are room for improvement in analysis of this paper. The following list shows the problems to be solved and future plans.

- Further optimization of event selection criteria.(Especially on D^{*+} , B^+)
- Further study on the treatment of background. We have to check the validity to use same resolution function of Δz on signal and background.
- Study on the vertexing method of the other B decay for the improvement of the Δz resolution.
- Development of method to take into account of tracking errors on event by event.
- Systematics study.

Bibliography

- [1] BELLE collaboration. A study of cp violation in b meson decays — technical design report. Technical Report 1, KEK, 1995.
- [2] Particle Data Group. Review of particle physics. *The European Physical Journal C*, 3(1-4):1–794, 1998.
- [3] Dan Payne Sawako Nakanishi, Hiro Tajima. A model independent measurement of the $d_s^- \rightarrow \phi\pi^-$ branching fraction. *CBX*, (67):7, August 14 1995.
- [4] JUN-ICHI TANAKA. Kinematic fitting. *BELLE note*, (194), March 15 1998.

Acknowledgment

At First I would like to express my great thank to the Supervisor H.Aihara. I am deeply thankful to H.Tajima for his powerfull support in my studies. My thanks go to all the members to BELLE SVD group for their support and suggestions in my study and my life in KEK. I greatly appreciate many discussions with all the students of our lab, J.Tanaka, M.Yokoyama, T.Highchi, T.Matsubara and T.Tomura. At the last I would like to the everyone supporting me.